Applied Ocean Research 90 (2019) 101843

Contents lists available at ScienceDirect

Applied Ocean Research

journal homepage: www.elsevier.com/locate/apor

# Effects of wave directionality on extreme response for a long end-anchored floating bridge

Thomas Viuff[a,*], Bernt Johan Leira[a], Xu Xiang[b], Ole Øiseth[c]

[a] Department of Marine Technology, Norwegian University of Science and Technology, N-7491 Trondheim, Norway
[b] Norwegian Public Roads Administration, N-0667 Oslo, Norway
[c] Department of Structural Engineering, Norwegian University of Science and Technology, N-7491 Trondheim, Norway

ARTICLE INFO

*Keywords:*
Floating bridge
Von Mises stress
Short-term extreme response
Accuracy in extreme response prediction
Main wave direction
Spreading exponent

ABSTRACT

Reliable design codes are of great importance when constructing new civil engineering concepts such as floating bridges. Previously only a scarce number of floating bridges have been built in rough wave conditions and only limited knowledge of the extreme environmental conditions and the associated extreme response exists. To form a better design basis an increased understanding of the sensitivity in the structural response towards changes in short-crested sea parameters is needed. Furthermore, acquiring the necessary accuracy in simulated extreme response is often a computationally expensive endeavour and the number of simulations needed is often based on experience. The present study investigates the wave-induced short-term extreme response of a simplified end-anchored floating bridge concept for several wave environments with a return period of 100 years. The study includes convergence of the coefficient of variation for the extreme response for different realization lengths as well as number of realizations. The sensitivity in the structural response towards different main wave directions and spreading exponents is investigated and includes both transverse and vertical displacement response spectra and extreme Von Mises stress in the bridge girder cross-section. The extreme response is based on an accuracy of 2% in the coefficient of variation equivalent to 40 3-h realizations and a low sensitivity in the response is found for natural occurring spreading exponents and for main wave directions within 15° from beam sea.

## 1. Introduction

The Norwegian Public Roads Administration (NPRA) is currently undertaking a large infrastructure project involving floating bridge structures over their wide and deep fjords. The fjords are up to 1300 m deep, 6000 m wide and located in the western part of Norway exposing the structures to rough wind and wave conditions from the North Sea. These extreme conditions make it important to understand the structural response and their sensitivity to changes in the wave environment. Stochastic wave loading processes and their application in stochastic response of floating bridges has been a research topic since the late 1970s and the structural response of a short (less than 1500 m) curved floating bridge with continuous pontoons was thoroughly investigated in the late 1970s and the 1980s [1–6] when construction of the Bergsøysund Bridge and the Nordhordland Bridge was under way. The studies included both time domain and frequency domain analyses and included regular waves, irregular long-crested waves and short-crested waves. Sigbjörnsson [2] described an explicit representation of the short-crested behaviour of waves in the frequency domain. Coherency functions were used to show the correlation between wave loads as a function of the spreading exponent and the spatial coordinates, based on previous research by Borgman [7]. Langen and Sigbjörnsson [3] applied the directional wave spectrum in time domain and concluded that a design using long-crested waves would yield unreasonably conservative results, whereas for short-crested waves a low sensitivity was found in the response towards changes within naturally occurring spreading exponent values. Hutchison [8] showed that a logical consistency existed between the two principal methods existing at the time for describing the dynamic response from short-crested waves, i.e. superposition of long-crested waves and an explicit representation of the short-crested behaviour of the incident wave field such as the one described by Sigbjörnsson [2]. Another method to give an explicit representation of the wave field mentioned by Hutchison was the use of an empirical *spacial correlation factor* described by Hartz and Georgiadis as a reduction factor for the time series of nodal wave forces in a numerical analysis [8]. Langen and Leira [4–6] carried out several studies on the probabilistic design of the short floating bridge structure focusing on the bending moments and pre-tension force in the bridge

* Corresponding author.
*E-mail address:* thomas.h.viuff@ntnu.no (T. Viuff).

https://doi.org/10.1016/j.apor.2019.05.028
Received 31 October 2018; Received in revised form 24 May 2019; Accepted 29 May 2019

cross-section. The studies found that the correlation between the bending moments was important to take into account and that it was dependent on the peak period in the wave spectrum. In more recent years Villoria [9] found a lower influence in the response from changes in the spreading exponent and the wave spectrum shape than from changes in the wave direction and wave period for a long (more than 4000 m) straight and a curved floating pontoon bridge.

For many engineering purposes the design wave parameters are taken as valid inputs but as Moan et al. [10] describes, generally for marine structures the extreme response is very sensitive to the amount of data available to represent the long-term variability of the wave conditions. Bitner-Gregersen et al. [11] noted that some epistemic (knowledge based) uncertainties related to environmental descriptions of wind and waves exists, such as non-stationarity, sampling variability and directionality of wind and waves. A comparison of three metocean databases is described in Bitner-Gregersen et al. and the difference in the significant wave height and the zero-crossing period for return periods of 100 years was found to be over 5 m and 4 s, respectively. Another issue argued by Bitner-Gregersen et al. is the frequency-dependent behaviour of the directional spreading in in-situ measurements. Other uncertainties related to in-situ measurements are pointed out by Kvåle and Øiseth [12] who describes the differences in identification methods for characterizing the wave field based on simulated data. They conducted a comparison of two identification methods using three different sensor layouts and found clear differences in the methods for the sensor layouts they used. These uncertainties all relate to the design wave environment and a thorough understanding of the sensitivity in the extreme floating bridge response is needed in order to quantify the importance of these uncertainties.

The extreme response for long floating bridge structures is a topic touched upon in recent years. Giske et al. [13] have compared the environmental contour method with the full long-term extreme method for a long double-curved floating pontoon bridge and found that it can give a rough estimate of the real long-term extreme response. Giske et al. also compared a new Inverse Second Order Reliability Method (ISORM) described in [14] to the full long-term extreme method and found it to give a high accuracy in the long-term extreme response. Øiseth et al. [15] compared the Average Conditional Exceedance Rates (ACER) method described in [16] to the Gumbel method for the extreme response for a short curved floating pontoon bridge and found that the ACER method had a significantly narrower confidence interval, introducing less uncertainty in the estimation of the extreme response. Xu et al. [17] compared two short-term extreme methods based on the ACER method to a full long-term extreme method for a single-span suspension bridge and found the extreme load effects from the full long-term extreme method to be 14% higher.

With the rough wave conditions at the Bjørnafjord and the described uncertainties in the estimation of the wave parameters, it is important to understand the structural response and the effect of changes in these parameters on the extreme response. The current paper presents an extensive numerical study of the extreme response for a long end-anchored floating pontoon bridge with emphasis on the needed simulation length and number of realizations in order to achieve the necessary accuracy and a parametric study of the extreme response based on the main wave direction and the spreading exponent for short-crested sea. To the knowledge of the authors, all previous studies on the sensitivity of the extreme response to the wave directionality has either been conducted in frequency domain or on a few short time domain simulations. In the present paper it is the first time a numerical parameter study is based on an extensive amount of time domain simulations for each changed parameter and will help solidify the understanding of their effect on the extreme response of a long floating bridge. As part of the extensive time domain calculations the dependency of the accuracy in the short-term extreme prediction towards the simulation length and the number of realizations has been investigated for the general floating bridge structure to be used as a reference for future investigations of the extreme response.

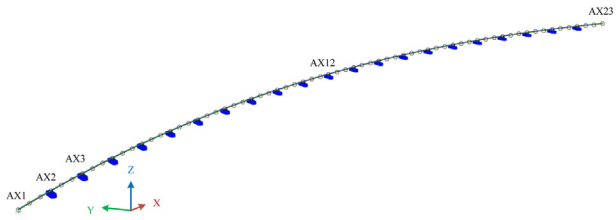


**Fig. 1.** Numerical model of the end-anchored floating bridge.

## 2. Description of the floating bridge concept

The floating bridge modelled in the present study is a simplification of the Bjørnafjord end-anchored floating bridge concept described by COWI [18]. The simplified concept seen in Fig. 1 consists of a double-symmetric twin-box cross-section bridge girder at roughly 15 m height, covering roughly 4360 m of roadline and has a curvature of 5000 m in the horizontal plane. The bridge girder is connected to 21 floating pontoons every 197 m with two circular columns. The pontoons are the only part of the bridge in contact with the water and the bridge girder is connected to the shore at each end of the bridge, modelled as fixed connections. The bridge girder and the columns are modelled as single equivalent beams in the numerical model with the cross-sectional properties listed in Table 1.

The pontoons all consist of the same geometry, draft and hydrodynamic coefficients. Looking at a pontoon from above, the geometry is made up of two half circles with a rectangle in between, see Fig. 2. The total length is 68 m, the total width is 28 m and the height is 14.5 m with a draft of 8.8 m found from static equilibrium. For all the pontoons surge follows the global $x$-axis and sway follows the global $y$-axis as shown in Fig. 2. Throughout this paper indices one to six for hydrodynamic coefficients indicate surge, sway, heave, roll, pitch and yaw accordingly. Table 2 lists the properties of the pontoon. Based on the bridge girder mass in Table 1 and the pontoon mass and displacement in Table 2 the static equilibrium can be verified.

## 3. Methodology

The aim of the paper is two-fold: (1) to find the required realization length and number of realizations to achieve a reliable accuracy in the extreme response and (2) to describe the effect of changing short-crested sea parameters on the extreme response. In the following a description is given of the numerical model as well as the assumptions made in order to calculate the stresses in the bridge girder from the internal forces given as output in the numerical model. Later on the choice of parameters to be changed in the parametric study is argued and finally a description is given of how the extreme response is estimated and how the necessary accuracy is achieved.

**Table 1**
Single equivalent beam cross-section properties [18]. The notations $EI_y$ and $EI_z$ refer to the bending stiffness about the weak and strong axis, respectively, and the notation $EA$ refer to the axial stiffness. Similarly the notations $GI_x$ and $r_x$ refer to the torsional stiffness and the radius of gyration, respectively.

| Property | Unit | Girder | Column |
|---|---|---|---|
| Mass | [ton/m] | 2.67E+01 | 1.60E+01 |
| $r_x$ | [m] | 2.02E+01 | 1.84E+01 |
| $EA$ | [kN] | 3.87E+08 | 3.68E+08 |
| $EI_y$ | [kNm$^2$] | 2.76E+09 | 2.92E+09 |
| $EI_z$ | [kNm$^2$] | 1.56E+11 | 1.29E+11 |
| $GI_x$ | [kNm$^2$/rad] | 6.10E+10 | 5.07E+10 |

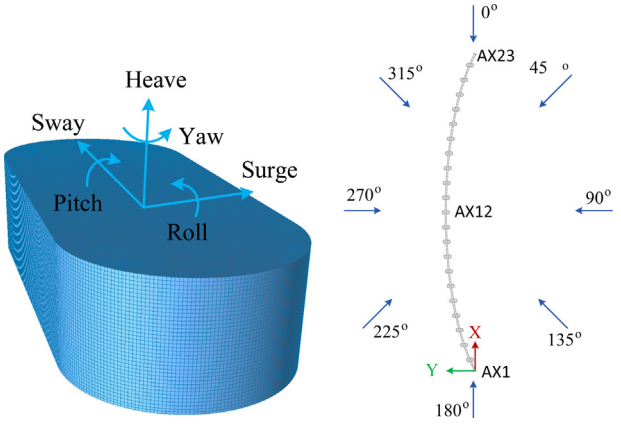


**Fig. 2.** Pontoon panel model and body-fixed coordinate system (left) and compass notation of wave directions and global coordinate system (right).

**Table 2**
Pontoon properties [18].

| Property | Unit | Value |
|---|---|---|
| Mass | [ton] | 1.03E+04 |
| Roll inertia | [ton m$^2$] | 4.93E+06 |
| Pitch inertia | [ton m$^2$] | 1.21E+06 |
| Yaw inertia | [ton m$^2$] | 5.47E+06 |
| COG from waterline | [m] | −2.53E+00 |
| Displacement | [ton] | 1.57E+04 |
| Roll water plane stiffness | [kNm/rad] | 5.33E+06 |
| Pitch water plane stiffness | [kNm/rad] | 6.18E+05 |
| Heave stiffness | [kN/m] | 1.75E+04 |

### 3.1. Numerical model

The numerical model of the floating bridge is developed in the coupled hydro-elastic code SIMO-RIFLEX [19,20]. The structural system is idealized using the Finite Element Method (FEM) with the bridge girder and the columns modelled as Euler-Bernoulli beams and the pontoons as 6 degrees of freedom (DOF) nodes with hydrodynamic mass, stiffness and damping properties. The bridge girder is fixed at each end in all DOF. The mesh of the model is made up of girder elements of roughly 5 m and column elements of roughly 3 m lengths, resulting in a total of roughly 950 beam elements in the model. The hybrid frequency- and time domain model is utilized in the code to set up the equation of motion commonly known as the Cummin's equation [21,22].

$$\begin{aligned} & q_j^{\mathrm{exc}}(t) \\ & = \sum_{k=1}^{6} [M_{\mathrm{jk}} + A_{\mathrm{jk}}^{\infty}]\ddot{u}_k(t) + D_{\mathrm{jk}}\dot{u}_k(t) \\ & \quad + [K_{\mathrm{jk}} + C_{\mathrm{jk}}]u_k(t) + \int_0^{t_{\mathrm{mem}}} k_{\mathrm{jk}}(t-\tau)\dot{u}_k(\tau)d\tau \end{aligned} \tag{1}$$

Here, $M_{jk}$, $D_{jk}$ and $K_{jk}$ are the structural mass-, damping-, and stiffness matrix, respectively, and $C_{jk}$ is the hydrostatic stiffness matrix. The hydrodynamic added mass $A_{\mathrm{jk}}(\omega) = A_{\mathrm{jk}}^{\infty} + a_{\mathrm{jk}}(\omega)$ is here divided into a frequency-independent part $A_{\mathrm{jk}}^{\infty}$ corresponding to the added mass at infinite frequency and a frequency-dependent term $a_{jk}(\omega)$. The same goes for the hydrodynamic damping $B_{\mathrm{jk}}(\omega) = B_{\mathrm{jk}}^{\infty} + b_{\mathrm{jk}}(\omega)$. The notation $\omega$ here refers to angular frequency. The indices are defined according to the body-fixed coordinate system with $j = 1, 2, \ldots$ signifying surge, sway and so forth. The wave excitation force $q_j^{\mathrm{exc}}(t)$ is a combination of the Froude-Krylov force and the diffraction force from solving the diffraction problem and is equivalent to the first order wave force $q_j^{(1)}(t)$. The displacement and its time derivatives are symbolized with $u_k(t)$, $\dot{u}_k(t)$ and $\ddot{u}_k(t)$ with $t$ referring to time and $\tau$ representing the time lag in the convolution within the "memory" time $t_{mem}$. The hydrodynamic frequency-dependent added mass and damping found by solving the radiation problem are included in Eq. (1) through the retardation function $k_{jk}(t)$.

$$\begin{aligned} k_{\mathrm{jk}}(t) &= \frac{1}{2\pi}\int_{-\infty}^{\infty}[b_{\mathrm{jk}}(\omega) - i\omega a_{\mathrm{jk}}(\omega)]e^{i\omega t}d\omega \\ &= \frac{2}{\pi}\int_0^{\infty} b_{\mathrm{jk}}(\omega)\cos(\omega t)d\omega \end{aligned} \tag{2}$$

Here $i$ is the imaginary unit. The retardation function $k_{jk}(t) = 0$ for $t < 0$ due to causality and $k_{jk}(t) \to 0$ for $t \to \infty$. The last term in Eq. (2) is derived by expanding the complex notation, removing the odd parts of the equation and applying the causality property. The frequency-independent damping $B_{\mathrm{jk}}^{\infty}$ is zero since physically no waves are generated when the structure is oscillating at infinite frequency.

#### 3.1.1. Modelling the first order wave load

The sea surface elevation consists of wind-generated waves approximated as a stationary and homogeneous random field. The wind-generated waves are described by a directional wave spectrum $S_\zeta(\omega, \theta)$ approximated as the product of the unidirectional wave spectrum $S_\zeta(\omega)$ and the directional spreading function $D_\zeta(\theta)$. The JONSWAP [23] wave spectrum in Eq. (3) is applied in the analysis.

$$S_\zeta(\omega) = \frac{\alpha g^2}{\omega^5}\exp\left(-1.25\frac{\omega_p^4}{\omega^4}\right)\gamma^{\exp\left(-\frac{(\omega-\omega_p)^2}{2\beta^2\omega_p^2}\right)} \tag{3}$$

The spectral parameters $\alpha$ and $\beta$ are, for North Sea projects, often defined as $\alpha = 5.061H_s^2T_p^{-4}[1 - 0.287\ln(\gamma)]$ and $\beta = 0.07$ for $\omega \le \omega_p$ or $\beta = 0.09$ for $\omega > \omega_p$, respectively. $g$ is the gravitational acceleration and the remaining variables are the peak angular frequency $\omega_p$, the peakedness parameter $\gamma$ and the significant wave height $H_s$. The directional spreading function is given in Eq. (4) where $\theta$ is the wave direction, $\theta_0$ is the main wave direction, $s$ is the spreading exponent and $\Gamma(\cdot)$ is the Gamma function.

$$D_\zeta(\theta) = \frac{1}{\sqrt{\pi}}\frac{\Gamma(\frac{s}{2}+1)}{\Gamma(\frac{s}{2}+\frac{1}{2})}\cos^s(\theta-\theta_0), \quad |\theta-\theta_0| \le \frac{\pi}{2} \tag{4}$$

The first order wave force is generated by Monte Carlo simulation using fast Fourier transformations (FFT) of the real part $\Re(\cdot)$ of the first order wave force transfer function $H_j^{(1)}(\omega_m, \theta_n)$ and the wave spectrum $S_\zeta(\omega_m)$.

$$\begin{aligned} q_j^{(1)}(\mathrm{x},\mathrm{y},\mathrm{t}) \quad &= \Re\sum_{m=1}^{N_\omega}\sum_{n=1}^{N_\theta}\sqrt{2S_\zeta(\omega_m)D_\zeta(\theta_n)\Delta\omega_m\Delta\theta_n} \\ &\quad |H_j^{(1)}(\omega_m,\theta_n)|\exp\left[i\left(\varepsilon_{\mathrm{nm}} + \varphi_{H_{\mathrm{jnm}}^{(1)}}\right)\right] \\ &\quad \exp[i(\omega_m t - k_m x\cos(\theta_n) - k_m y\sin(\theta_n))] \end{aligned} \tag{5}$$

Where $k_m$ is the wave number, $\varepsilon_{nm}$ is the random phase angle and $\varphi_{H_{\mathrm{jnm}}^{(1)}}$ is the phase angle.

The JONSWAP wave spectrum is used to describe the wave elevation with the parameters listed in Table 4. These parameters represents the preliminary wave condition at the Bjørnafjord for a 100-year return period [18]. The main wave direction follows the compass notations illustrated to the right in Fig. 2.

The hydrodynamic properties of the pontoon are found using the Boundary Element Method software Wadam [24]. With the extreme wave conditions located inside the Bjørnafjord the design wave height and wave period are still relatively small in comparison to the pontoon dimensions. For these specific wave conditions and pontoon geometry the structure is classified as a large structure with mainly diffraction loads being important. Utilizing the concept of double-symmetry the panel model used is one quarter of the pontoon. The panel model is given a general mesh size of 0.4 m resulting in a total of 5450 panel elements. The wave directions used are going from 90° to 180° with a 5°

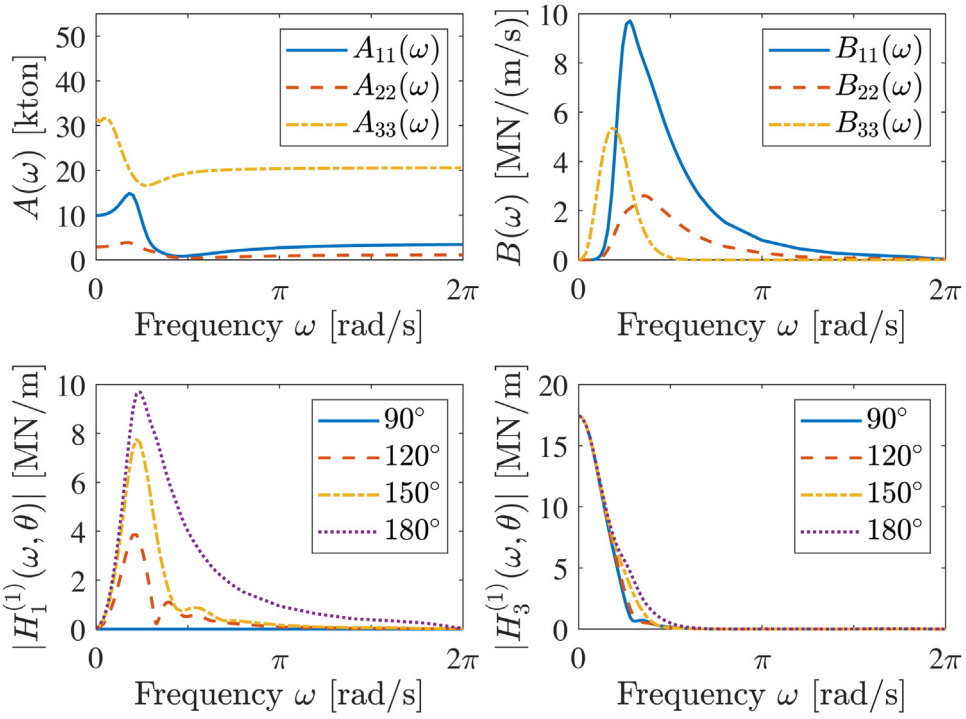


**Fig. 3.** Hydrodynamic coefficients following the body-fixed coordinate system of the pontoon with wave direction notation according to Fig. 2, i.e. waves from 90° and 180° follow sway and surge in the body-fixed coordinate system, respectively.

resolution following the notation in Fig. 2. Similarly the wave frequencies are between $2\pi/1000$ to $6\pi$ rad/s with varying frequency step (from $\Delta\omega = 2\pi/100$ at the lowest frequencies, to $\Delta\omega = 2\pi$ at the highest frequencies) in order to represent the hydrodynamic coefficients sufficiently. Fig. 3 illustrates the hydrodynamic properties of the pontoon. Noticeable information from Fig. 3 is the variation in the first order wave force transfer function for heave $|H_3^{(1)}(\omega, \theta)|$ within the frequency range of the wave spectrum for different wave directions.

In the hydrodynamic analysis of the pontoon the stiffness of the bridge superstructure is not taken into account. The solution of the classic radiation problem and diffraction problem does not depend on the pontoon stiffness and will not affect the hydrodynamic coefficients or the first order wave load transfer function. The first order motion transfer function, however, is affected but is not used in the estimation of the wave loads or the general response of the bridge. Instead the stiffness of the bridge superstructure is taken into account in the time domain analysis carried out in SIMO-RIFLEX. In other words, here the hydro-elasticity is only influencing the motions and responses, not the hydrodynamic coefficients in the model. The influence on motions may become more important when considering second order loads, but that is out of the scope of the present paper.

The option of modelling the wave loads as functions of spatial coordinates is built into the code. However, the correlation of the wave elevation at the different pontoon locations is significantly influenced by the irregular behaviour and the wave spreading. For short-crested beam sea the correlation is insignificant as pointed out by Kvåle et al. [25]. The almost non-existing correlation suggests that the wave forces acting on the pontoons could instead have been modelled as 21 independent wave loads.

In practice, the relative dimensions of the pontoons compared to the distance between them will govern whether the interaction effects should be accounted for or not. A simple estimation for hydrodynamic interaction between two ships is described in Xiang [26]. Based on this simplified estimation the interaction effects are assumed to be negligible for the present case study. Other studies have been made on floating bridges accounting for the hydrodynamic interaction effects such as Xiang et al. [27] and Seif and Inoue [28].

#### 3.1.2. Tidal variation

The tidal variation is ± 0.75 m from the mean sea level. An expected increase in the mean sea level of 0.8 m is expected in the future due to climate change [29]. Any effects of the tidal variations are assumed to be a static effect and for this reason is neglected in the present study.

#### 3.1.3. Note on using single equivalent beams

Both the bridge girder and the connection between the bridge girder and each pontoon are modelled as equivalent single beams with the cross-section properties listed in Table 1. When extracting the internal forces in the post-processing the effect of local stresses is neglected. For instance the stresses in the weld between the bridge girder and each column is not considered when calculating the stresses in the bridge girder.

#### 3.1.4. Structural damping

In the numerical model the structural damping is applied globally using Rayleigh damping. The mass and stiffness proportional damping coefficients are 0.01208 and 0.03061, respectively, resulting in a damping ratio between 0.02 and 0.03 within the frequency range of the wave spectrum. With a damping ratio of less than 0.02 for standard civil engineering structures the chosen damping ratio is on the un-conservative side. However, given the simplifications already listed, the present study is not focused on the correct modelling of the bridge but rather on the sensitivity of the extreme response towards the short-crested sea parameters. Furthermore, the choice of the increased damping ratio can be argued by the exclusion of other damping effects such as the viscous drag on the pontoons and the aerodynamic damping from wind. For instance, Wang et al. [30] showed that for a floating multi-span suspension bridge the aerodynamic damping from the wind significantly dampened the wave-induced response.

In the present study the Rayleigh damping applied with the mentioned coefficients is furthermore of low influence to the response due

to the large amount of potential hydrodynamic damping stemming from the pontoons.

#### 3.1.5. Solution procedures

The theory of the FEM is well established and hence only a general description of the solution procedures are given in the current section. For more details, the reader is referred to [20,31–33]. The solution $u(t)$ to the global system, i.e. the response time history, is first found based on a Newmark time step integration procedure and a Newton-Raphson iteration within each time step. The internal forces and moments at each time step are then found using the theory of virtual work using the global displacements and rotations at the end nodes of each individual beam element in the system together with the stress-strain relationships and the element interpolation functions. As an example, the internal weak axis bending moment $M_y$ is found through the following integration over the initial element length $L_0$.

$$M_y = \int_{L_0} N''^{T}_{z,xx} \mathrm{EI}_y \kappa_y \mathrm{d}x \tag{6}$$

Where $N''^{T}_{z,xx}$ is the transpose of the vector of second derivatives with respect to the longitudinal direction x of the cubic interpolation functions for the transverse displacement z for a beam element. The remaining quantities $\kappa_y$ and $EI_y$ refer to the curvature and the bending stiffness around the y-axis, respectively.

Static equilibrium is obtained using an incremental loading of the static forces in the system. At each incremental step the Newton-Raphson iterative procedure is used to find convergence [20].

For solving the standard eigenvalue problem SIMO-RIFLEX uses the iterative Lanczos Method. The build-in procedure makes use of the hydrostatic stiffness and the hydrodynamic added mass at infinite frequency for the pontoons in the solution. Table 3 lists a manual pseudo-procedure used in order to take into account the frequency-dependent added mass in the solution.

Stability of the time-domain solution is obtained by specifying a ramping time of 10 s and a time step of 0.05 s based on an initial convergence study.

### 3.2. Parametric study

A parametric study is carried out in order to investigate the sensitivity of the response to the different naturally occurring spreading exponents and main wave directions.

#### 3.2.1. Load cases for short-crested sea

A total of 12 load cases are specified for the parametric study listed in Table 4. They are made up of two main groups with different spreading exponents for normal occurring short-crested sea. For each group the main wave direction is changed. Due to a strong linear relationship between the response and the wave height a constant significant wave height is specified in the study. The peak period of the wave spectrum is also kept constant in the current study, although Larssen et al. [34] has shown that the peak period has a significant effect on the probability of failure for a curved submerged floating tube bridge (SFTB). While the significance of the peak period for the response most probably is transferable to a floating pontoon bridge the parameter has been kept constant due to time considerations.

**Table 3**
Manual pseudo procedure for solving the standard eigenvalue problem when accounting for frequency-dependent added mass.

**INPUT** $N$, $A(\omega)$, tolerance
Solve $[K - \omega^2(M + A^{\infty})]\psi = 0$
Store the first $N$ natural angular frequencies as $\omega_n$
**FOR** $n$ = 1 to $N$
  $\omega_{out} = \omega_n$
  diff = tolerance + 1
  **WHILE** diff > tolerance
$\omega_{in} = \omega_{out}$
Solve $[K - \omega^2(M + A(\omega_{\mathrm{in}}))]\psi = 0$
Store the $n$'th natural angular frequency as $\omega_{out}$
diff = $|\omega_{\mathrm{in}} - \omega_{\mathrm{out}}|$
  **END**
  Store $\omega_{out}$ as $\omega_n^*$
**END**

**Table 4**
Load cases used in the parametric study. First order wave loads are applied with the chosen JONSWAP parameters $H_s$ = 3.0 m, $T_p$ = 6.0 s and $\gamma$ = 3.3 based on the wave conditions at the Bjørnafjord for a 100-year return period [18].

| Load case | Spreading | Wave direction | Load case | Spreading | Wave direction |
|---|---|---|---|---|---|
| LC1.1 | 2 | 90° | LC2.1 | 10 | 90° |
| LC1.2 | 2 | 95° | LC2.2 | 10 | 95° |
| LC1.3 | 2 | 100° | LC2.3 | 10 | 100° |
| LC1.4 | 2 | 105° | LC2.4 | 10 | 105° |
| LC1.5 | 2 | 120° | LC2.5 | 10 | 120° |
| LC1.6 | 2 | 150° | LC2.6 | 10 | 150° |

#### 3.2.2. Estimating Von Mises stress in bridge girder

From the global analysis only internal forces are extracted from the numerical model. In the post-processing of the results the internal forces are used as input to calculate the Von Mises stress $\sigma_v(t)$ in the bridge girder. Fig. 4 illustrates the basic assumptions made in order to estimate the Von Mises stress. One such assumption is the shear forces and torsional moments being divided equally among the two boxes in the twin-box cross-section. The second assumption is that the shear flow from the torsional force follows the contour of each box cross-section. This assumption is based on Damkilde [35] stating that the torsional shear flow is constant over a closed thin-walled cross-section. With the assumed distribution of the internal forces Eq. (7) is used to calculate the Von Mises stress at each time step $t$.

$$\sigma_v(t) = \sqrt{\sigma_{\mathrm{xx}}^2(t) + 3(\tau_{\mathrm{xy}}(t) \pm \tau_{\mathrm{xz}}(t) \pm \tau_{\mathrm{xx}}(t))^2} \tag{7}$$

Here $\sigma_{xx}(t)$ is the normal stress, $\tau_{xy}(t)$ and $\tau_{xz}(t)$ are the shear stress from the horizontal and vertical shear force $S_y(t)$ and $S_z(t)$, respectively. The torsional shear stress $\tau_{xx}(t)$ is associated with the torsional moment $M_x(t)$. The sign convention used depends on the direction of the shear flow as illustrated in Fig. 4.

The normal stress is found using Eq. (8) with the internal forces being the effective tension $T_e(t)$, the weak axis bending moment $M_y(t)$ and the strong axis bending moment $M_z(t)$. The total cross-sectional area of the twin-box cross-section is given by $A_x$ and the notations $y$ and $z$ are the distance between the neutral axes of the twin-box cross-section and the point in question. The second moment of area $I_y$ and $I_z$ of the twin-box girder are around the two neutral axes indicated by the index.

$$\sigma_{\mathrm{xx}}(t) = \frac{T_e(t)}{A_x} + \frac{M_y(t)z}{I_y} - \frac{M_z(t)y}{I_z} \tag{8}$$

The shear stresses $\tau_{xy}(t)$ and $\tau_{xz}(t)$ in the local $y$ and $z$ direction, respectively, are found using Eqs. (9) and (10) for points located $y_d$ or $z_d$ from the neutral axes. In the case of calculating $\tau_{xz}(t)$ at the point $z_d$ from the neutral axis $\bar{A}$ is the area of the cross-section from the point to the top of the box as illustrated in Fig. 4. Similarly $\bar{z}$ is the centroid of that given area measured from the neutral axis. The torsional shear stress $\tau_{xx}(t)$ is given by Eq. (11) with $t_w$ being the thickness of the girder wall at the point of interest and $A_c$ is the enclosed area of a single box girder.

$$\tau_{\mathrm{xy}}(t) = \frac{S_y(t)}{2}\frac{\bar{A}_y\bar{y}}{I_z t_w} \tag{9}$$

$$\tau_{\mathrm{xz}}(t) = \frac{S_z(t)}{2}\frac{\bar{A}_z\bar{z}}{I_y t_w} \tag{10}$$

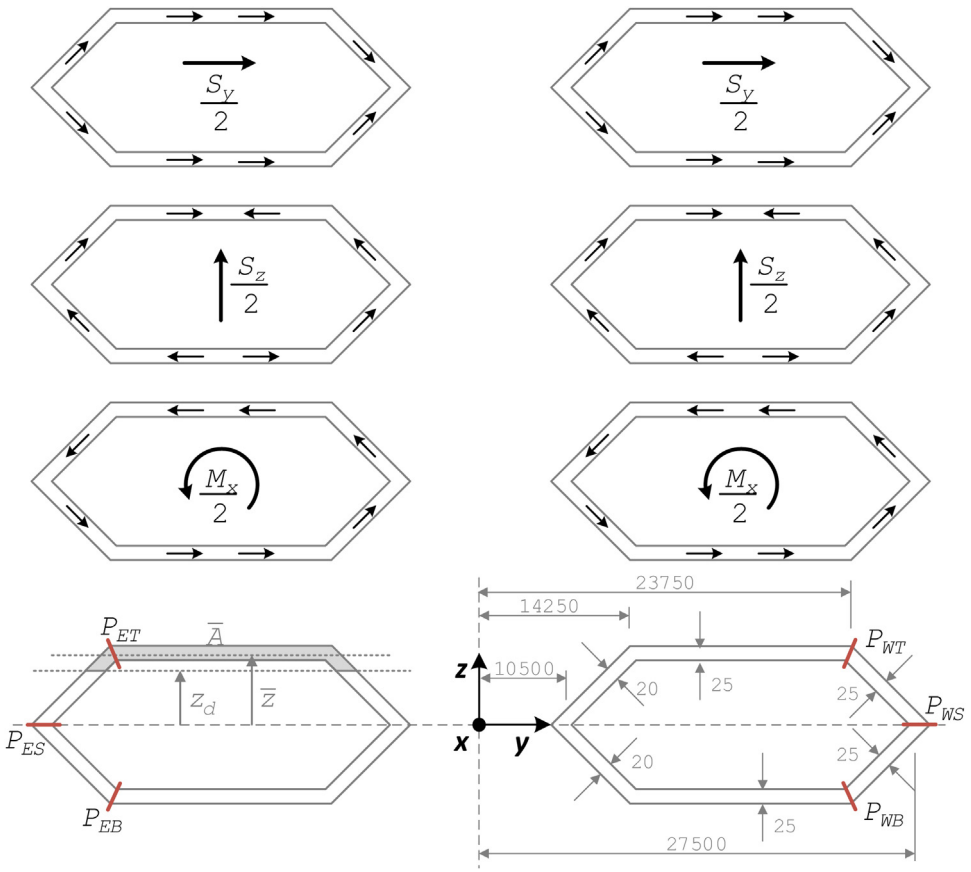


**Fig. 4.** Bridge girder cross-section with critical points and assumed stress distribution for calculating cross-sectional stresses. All measurements are in mm.

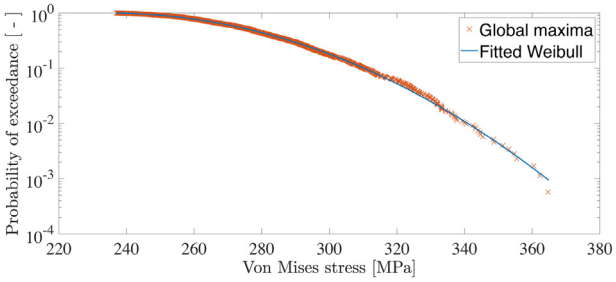


**Fig. 5.** Fit of a Weibull distribution to the global maxima Von Mises stress in point $P_{ET}$ at AX23 for LC1.1 from a single 3-h realization.

$$\tau_{xx}(t) = \frac{M_x(t)}{2}\frac{1}{2A_c t_w} \tag{11}$$

The six critical points in the bridge girder cross-section are $P_{WT}$, $P_{WS}$, $P_{WB}$, $P_{ET}$, $P_{ES}$ and $P_{EB}$ with the first index being $E$ or $W$ for eastern or western box. Similarly the second index is $T$, $S$ or $B$ short for top, side or bottom. The locations of the six critical points are shown in Fig. 4.

### 3.2.3. Extreme response prediction

Extreme response prediction of a structural system is dependent on the characteristics of the stochastic load and the (non)-linearity of the structural system. With only first order Gaussian waves acting on a linear structural system, the structural response can be considered Gaussian in nature with the local maxima of the time series following a Rice distribution (Rayleigh distribution for narrow-banded processes) and the largest maxima for several statistically independent realizations will hence follow a Gumbel distribution asymptotically. An initial investigation has been conducted with several regular wave scenarios with changing wave height in order to see if the structural response is linear. Even though SIMO-RIFLEX include non-linear behaviour such as geometric stiffness in the solution algorithm, the relationship between the wave height and the dynamic structural response was found to be linear. It then follows that the extreme response should follow a Gumbel distribution.

The extreme response is estimated using a short-term method according to recommendations given in Spidsøe and Karunakaran [36]. For a single realization of the response a Weibull distribution is fitted to the global maxima as recommended by Farnes and Moan [37] using the method of matching statistical moments. In order to predict the extreme response from extrapolation of the Weibull distribution a good fit to the global maxima in the upper tail is necessary. This is generally achieved using a threshold to avoid over representation of small maxima in the fitting procedure. The threshold is an empirical value and as pointed out by Fu et al. [38] can have a significant effect on the shape of the Weibull distribution. Using a threshold equal to the mean value of the time series the Weibull fits well to the global maxima as illustrated in Fig. 5.

Based on the number of global maxima $N_m$ in the time series and the Weibull location parameter $\delta$, scaling factor $\lambda$ and shape factor $\upsilon$ an estimate of the *extrapolated extreme* $\mu_{X_e}$ is calculated.

$$\mu_{X_e} = \delta + \lambda\left[(\ln(N_m))^{\frac{1}{\upsilon}} + \frac{0.57722}{\upsilon}(\ln(N_m))^{\frac{1-\upsilon}{\upsilon}}\right] \tag{12}$$

Based on $N_r$ realizations the *average extrapolated extreme* $\bar{\mu_{X_e}}$ and the corresponding standard deviation $\sigma_{\bar{X}_e}$ and coefficient of variation (c.o.v.) $C_{X_e}$ are found.

$$\bar{\mu_{X_e}} = \frac{1}{N_r}\sum_{i=1}^{N_r}(\mu_{X_e})_i \tag{13}$$

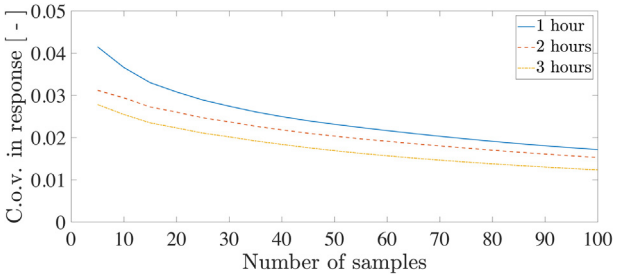


**Fig. 6.** C.o.v. of *average extrapolated extremes* vs simulation length and number of samples for Von Mises stress in point $P_{ET}$ at AX23 for LC1.1.

$$\sigma_{\bar{X}_e} = \sqrt{\frac{1}{N_r - 1}\sum_{i=1}^{N_r}\left(\left(\mu_{X_e}\right)_i - \mu_{\bar{X}_e}\right)^2} \tag{14}$$

$$C_{X_e} = \frac{\sigma_{\bar{X}_e}}{\mu_{\bar{X}_e}} \tag{15}$$

For load case LC1.1 the largest *average extrapolated extreme* of the Von Mises stress is observed to be in point $P_{ET}$ at axis AX23 on the bridge. Here a comparison of the c.o.v. of the *average extrapolated extreme* is performed for three sets of 100 realizations, each with the realization length of 1 h, 2 h and 3 h, respectively. In Fig. 6 the c.o.v. of the *average extrapolated extremes* is presented as a function of the realization length and the number of realizations. These results show that one will obtain a c.o.v. of less than 4% for even the shortest realization length using roughly 10 realizations. For a 3 h realization length 10 realizations give a c.o.v. of approximately 2.5% while 40 realizations give less than 2%. This is thought to be an acceptable level of accuracy. The Type I extreme value distributions obtained from the fitted Weibull parameters from 2 sets of 40 realizations are compared to the *sample extremes* as well as a Gumbel distribution fitted to the 100 *sample extremes* in Fig. 7. Based on the $-log(-log(\cdot))$ values of the cumulative distribution functions denoted with $F_x$ the two Type I distributions based on 40 independent 3 h realizations both show a good fit and will be used in the following parametric study for each load case listed in Table 4.

## 4. Results and discussion

### 4.1. Modal properties

Table 5 lists the natural frequencies of the structure with modes 3–30 in the range of the 100-year wave spectrum applied in the parametric study. Many of the active natural periods are within 0.1 s of each other, making the floating bridge a complex structural system. Fig. 8 shows the transverse and vertical displacements of the corresponding modeshapes when accounting for the frequency-dependent added mass, which have a significant effect on the weak and strong axis bending moment in the bridge girder. With the structural system being strongly

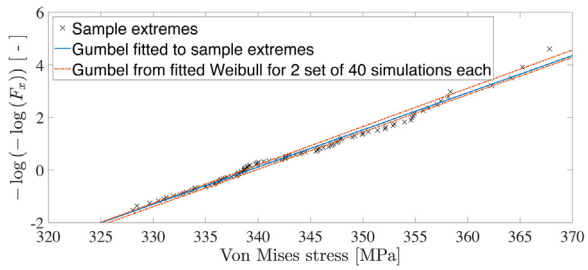


**Fig. 7.** Fit of *sample extreme* Von Mises stress in point $P_{ET}$ at AX23 for LC1.1 to the Gumbel distribution. They are compared to two Gumbel distributions obtained from fitted Weibull distributions.

**Table 5**
Eigenvalues of the floating bridge structure when accounting for frequency-dependent added mass ($\omega_n^*$) and when not ($\omega_n$). The corresponding modeshapes are of the same shape with insignificant differences.

| Mode $n$ | $\omega_n$ [rad/s] | $\omega_n^*$ [rad/s] | Mode $n$ | $\omega_n$ [rad/s] | $\omega_n^*$ [rad/s] |
|---|---|---|---|---|---|
| 1 | 0.133 | 0.126 | 16 | 0.732 | 0.780 |
| 2 | 0.232 | 0.220 | 17 | 0.750 | 0.801 |
| 3 | 0.396 | 0.372 | 18 | 0.773 | 0.826 |
| 4 | 0.441 | 0.409 | 19 | 0.799 | 0.854 |
| 5 | 0.671 | 0.620 | 20 | 0.828 | 0.887 |
| 6 | 0.685 | 0.726 | 21 | 0.861 | 0.899 |
| 7 | 0.685 | 0.726 | 22 | 0.896 | 0.918 |
| 8 | 0.686 | 0.726 | 23 | 0.910 | 0.922 |
| 9 | 0.686 | 0.727 | 24 | 0.920 | 0.957 |
| 10 | 0.687 | 0.728 | 25 | 0.929 | 0.992 |
| 11 | 0.690 | 0.731 | 26 | 0.960 | 1.023 |
| 12 | 0.693 | 0.735 | 27 | 0.985 | 1.048 |
| 13 | 0.699 | 0.741 | 28 | 1.000 | 1.064 |
| 14 | 0.707 | 0.751 | 29 | 1.229 | 1.257 |
| 15 | 0.718 | 0.764 | 30 | 1.393 | 1.438 |

linear the response is expected to be a superposition of the mode shapes and the Von Mises stress will in turn be affected by the contributions from the bending moments to the normal stress at the critical points of the girder cross-section. It should be noted that the modeshapes when *not* accounting for the frequency-dependent added mass show the same shape with insignificant differences. The corresponding frequencies, however, are slightly different.

### 4.2. Parametric study

In the following sections the sensitivity towards the main wave direction and the spreading exponent is summarized for the transverse and vertical displacement response spectra, the extreme Von Mises stress and the correlation between the weak and strong axis bending moment.

#### 4.2.1. Effect on displacement response spectra

Based on the time series of the transverse and vertical displacement at each axis the corresponding response spectra, $S_2(\omega)$ and $S_3(\omega)$ respectively, are found through a fast Fourier transformation (FFT) of the auto-correlation function of the said time series. This is done using WAFO [39] and the average of all 40 response spectra is used as the representative response spectrum for each load case. Although the response spectra are slightly different along the bridge the response spectra at the midspan illustrates the general effect at each pontoon. Figs. 9 and 10 show the changes in $S_2(\omega)$ and $S_3(\omega)$, respectively, towards the main wave direction and the spreading exponent for the midspan at AX12.

As a general observation, a low sensitivity in both response spectra towards the spreading exponent persists. The energy in $S_3(\omega)$ is only affected by the spreading exponent for main wave directions between 90° (beam sea) and 105°. Similarly, a low sensitivity towards the main wave direction is observed between beam sea and 105°. However, significant changes in $S_3(\omega)$ are observed for main wave directions larger than 105°.

Fig. 9 illustrates the changes in $S_3(\omega)$ for changing main wave direction and spreading exponent. Two main peaks are present corresponding to mode 21 and 22 of the structure (first peak) and the peak period $T_p$ of the wave spectrum (second peak). Although a slight shift is observed for the first peak this is too small to conclude anything about the relationship with the modeshapes. The first peak is significantly larger than the second peak and no peak is visible around mode 29. Instead a significant increase in the spectra around mode 26 is present for 150° even though the transverse displacement of this said mode is almost non-existing for AX12.

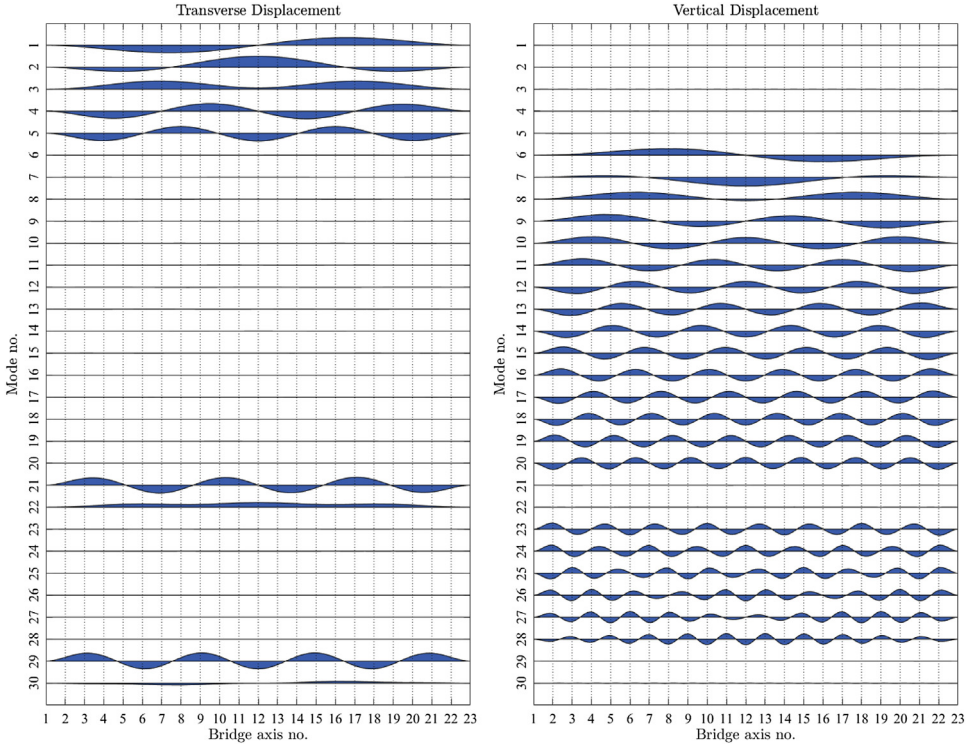


**Fig. 8.** Transverse and vertical displacement of the floating bridge modes based on exact added mass.

A low sensitivity in $S_3(\omega)$ towards the main wave directions between 90° and 150° is illustrated in Fig. 10. For these cases the spectra show a peak around mode 14 and 16 as well as at the peak corresponding to $T_p$ and mode 28. A significant increase in the overall energy is observed for main wave directions 120° and 150° and especially for the most short-crested seas does the peak at $T_p$ become more dominant. This behaviour is most likely related to the strong directional dependency in the first order wave force transfer function for heave $|H_3^{(1)}(\omega, \theta)|$ seen in Fig. 3. For frequencies between $2\pi/10$ and $2\pi/4$ rad/s corresponding to the frequencies within the applied wave spectrum the values for 150° are up to four times larger than the values for 90° (sway). In general, larger heave wave forces are present for directions closer to 180° (surge). A notable feature in $S_3(\omega)$ is the significant relative increase in the peak at $T_p$ for a main wave direction of 150° and although the larger heave force explains the general energy increase the first order wave transfer function for heave at 150° is only twice that for

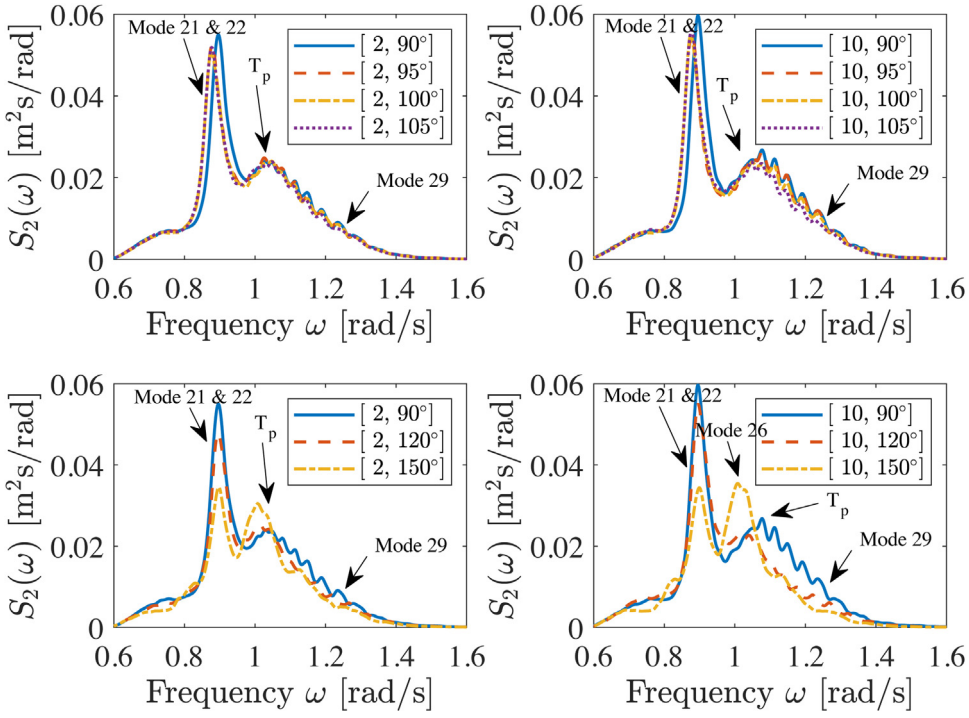


**Fig. 9.** Transverse response spectra of the bridge girder at the midspan AX12 for all load cases with different [$s$, $\theta_0$] values.

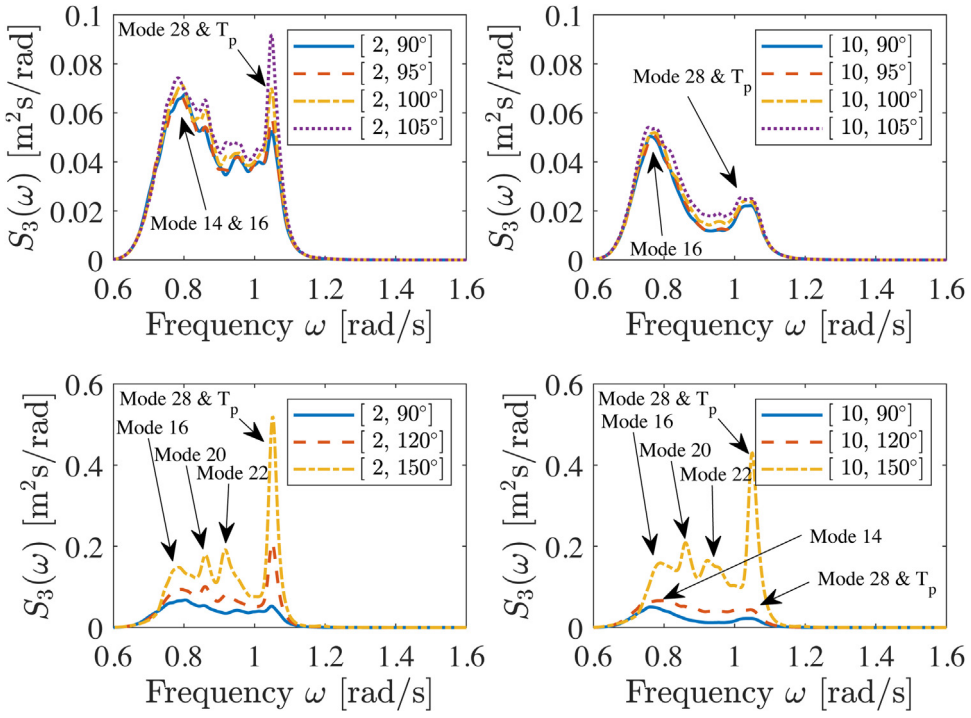


**Fig. 10.** Vertical response spectra of the bridge girder at the midspan AX12 for all load cases with different [$s$, $\theta_0$] values.

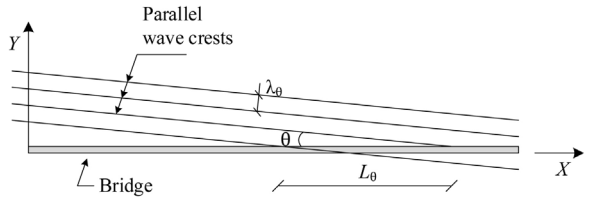


**Fig. 11.** Parallel wave crests propagating at an angle Θ from the normal of a straight bridge [40].

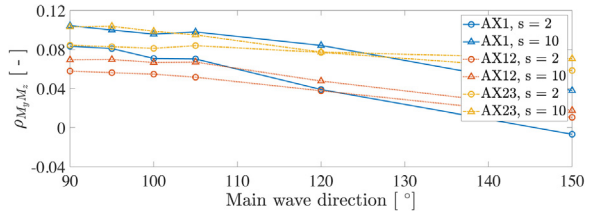


**Fig. 12.** Sensitivity in correlation of weak and strong axis bending moment to main wave direction and spreading exponent at specific points in the bridge.

heave at 90°. Remseth et al. [40] has described the principal effect of spacial resonance for a straight SFTB using regular long-crested waves at angles slightly different from beam sea. For a given regular wave with the frequency $\omega_8$ corresponding to the natural frequency of the 8th mode of the SFTB propagating at a specific angle Θ to the bridge normal as shown in Fig. 11 the distance $L_\Theta$ between the wave crests hitting the SFTB coincide with the peaks of the 8th modeshape of the structure and thereby amplifying the resonance effect. This effect is thought to be present in $S_3(\omega)$ at the midspan of the floating bridge in the current study, although it is difficult to verify systematically due to the many closely spaced natural periods of the structure and the neglected damping in the procedure to obtain said natural periods. Exposing the structure to long-crested regular waves at different wave directions with a wave period corresponding to a specific modeshape might work for low modes but in this case study the relevant modes are between 19 and 30. Furthermore, the strong directional dependency in the first

**Table 6**
Largest *average extrapolated extreme* Von Mises stress and their corresponding location in the bridge girder

| Load case | Axis | Point | Mean [MPa] | Std [MPa] | C.o.v. [%] |
|---|---|---|---|---|---|
| LC1.1 | AX23 | $P_{ET}$ | 371.9 | 4.1 | 1.1 |
| LC1.2 | AX23 | $P_{ET}$ | 372.2 | 3.6 | 1.0 |
| LC1.3 | AX23 | $P_{ET}$ | 374.0 | 3.7 | 1.0 |
| LC1.4 | AX23 | $P_{ET}$ | 375.7 | 4.4 | 1.2 |
| LC1.5 | AX23 | $P_{ET}$ | 383.3 | 5.6 | 1.5 |
| LC1.6 | AX23 | $P_{ET}$ | 404.7 | 6.0 | 1.5 |
| LC2.1 | AX23 | $P_{ET}$ | 364.9 | 4.0 | 1.1 |
| LC2.2 | AX23 | $P_{ET}$ | 365.7 | 4.5 | 1.2 |
| LC2.3 | AX23 | $P_{ET}$ | 366.3 | 3.4 | 0.9 |
| LC2.4 | AX23 | $P_{ET}$ | 365.8 | 3.7 | 1.0 |
| LC2.5 | AX23 | $P_{ET}$ | 373.2 | 6.0 | 1.6 |
| LC2.6 | AX23 | $P_{ET}$ | 408.0 | 6.6 | 1.6 |

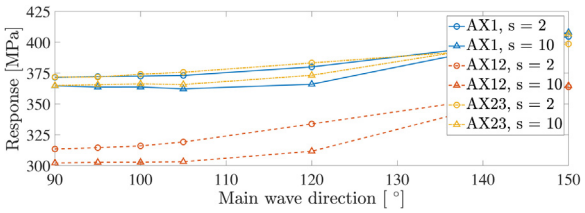


**Fig. 13.** Sensitivity in the *average extrapolated extreme* Von Mises stress in point $P_{ET}$ towards the main wave direction and the spreading exponent.

order wave load transfer functions will add further uncertainty to the results.

### 4.2.2. Effect on bending moment correlation

The weak and strong axis bending moments are generally important factors in the design of floating bridges as pointed out by e.g. Leira and Langen [6]. For the current structure the correlation coefficient $\rho_{MyMz}$ between the weak and strong axis bending moments is calculated for each realization within each load case listed in Table 4. The sensitivity

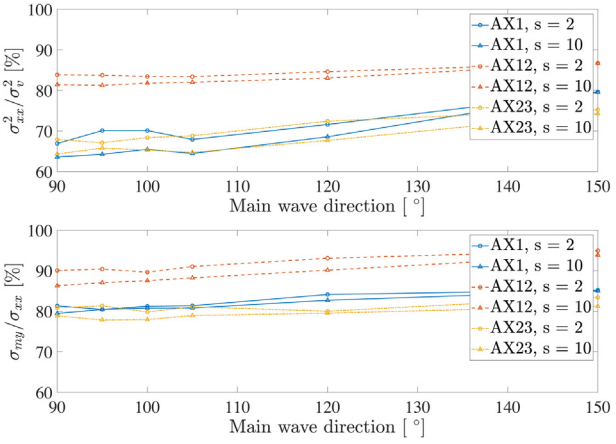


**Fig. 14.** Average contribution to *sample extreme* Von Mises stress at point $P_{ET}$ (top) and the associated normal stress (bottom).

towards changes in main wave direction and spreading exponent for the average correlation coefficient at the midspan and each end of the bridge is shown in Fig. 12. The correlation coefficient remains within 10% and seem to depend slightly on changes of both main wave direction and spreading exponent, although for main wave direction 90° and up to 105° the sensitivity towards the main wave direction is insignificant.

#### 4.2.3. Effect on extreme Von Mises stress

The Von Mises stress is evaluated at all six points shown in Fig. 4 and the value of the largest occurring *average extrapolated extreme* Von Mises stress for each load case is listed in Table 6 together with their corresponding location in the bridge. For all load cases the most critical point is in point $P_{ET}$ at AX23 in the bridge. The sensitivity in the response at this location is illustrated in Fig. 13 for changing main wave direction and spreading exponent showing that the *average extrapolated extremes* are within 10% for all load cases, except at AX12 for main wave direction 150° which is 20% larger. A relatively low sensitivity towards the spreading exponent is observed, although larger values are found for the most short-crested load cases. Similarly the main wave direction only has a measurable effect on the response for 120° and up. The observation of a low sensitivity towards the spreading exponent is supported by other studies made by Langen and Sigbjörnsson [3] who investigated the effect of short-crested sea in the design of a floating pontoon bridge.

In general $P_{ET}$ is found to be the most critical point in the cross-section for all load cases and at all axes along the bridge, except for AX20, AX21 and AX22 where $P_{WT}$ is the most critical. Fig. 14 illustrates the average contributions to the *sample extreme* Von Mises stress in point $P_{ET}$ at AX1, AX12 and AX23 for changing main wave directions and spreading exponents. The squared normal stress $\sigma_{xx}^2$ is the main contributor to the squared Von Mises stress $\sigma_v^2$ with at least 65% at the bridge abutments and up to 85% at the middle of the bridge. On average the largest contributor to the normal stress is the stress from the weak axis bending moment $\sigma_{my}$, which is responsible for roughly 80% of the normal stress at the two ends and up to 90% for the middle of the bridge.

## 5. Conclusion

A numerical study of the extreme wave-induced response for a long end-anchored floating bridge has been presented based on a short-term extreme method with a wave environment having a return period of 100 years.

The accuracy of the short-term extreme response method is investigated based on three sets of 100 realizations with realization lengths of 1 h, 2 h and 3 h, respectively. The coefficient of variation (c.o.v.) of the *average extrapolated extremes* from fitting Weibull distributions to realization maxima show clear dependency on both realization length and number of realizations. A chosen accuracy of less than 2% in the c.o.v. is achieved using 40 3-h realizations.

An extensive parametric study has been performed based on 40 3-h realizations for 12 different wave environments accounting for changing main wave direction and spreading exponent. A low sensitivity towards the spreading exponent is observed in the *average extrapolated extreme* Von Mises stress of the bridge girder and based on structural symmetry changes in the main wave direction are insignificant for directions within 15° from beam sea. The transverse and vertical response spectra show a similar behaviour, except for main wave directions more than 15° from beam sea where a significant change is observed. This effect is thought to be linked to spatial resonance described by Remseth et al. [40], although, the high structural complexity with several important natural periods within 0.1 s of each other makes it difficult to verify.

## Acknowledgements

This research was carried out with financial support from the Norwegian Public Roads Administration. The authors greatly acknowledge this support. We would also like to thank our colleague Ping Fu for her assistance in applying the extreme response prediction method used in the paper.

## References

[1] I. Holand, R. Sigbjörnsson, I. Langen, Dynamic analysis of a curved floating bridge, IABSE Proc. 1-16 (1977) P-5/77.
[2] R. Sigbjörnsson, Stochastic theory of wave loading processes, Eng. Struct. 1 (2) (1979) 58–64, https://doi.org/10.1016/0141-0296(79)90014-2.
[3] I. Langen, R. Sigbjörnsson, On stochastic dynamics of floating bridges, Eng. Struct. 2 (4) (1980) 209–216, https://doi.org/10.1016/0141-0296(80)90002-4.
[4] I. Langen, Probabilistic methods for dynamic analysis of floating bridges, Nor. Marit. Res. 11 (1) (1983) 2–15.
[5] B.J. Leira, Probabilistic Design – An Application to Floating Bridges, Tech. Rep., SINTEF, (1983).
[6] B.J. Leira, I. Langen, On probabilistic design of a concrete floating bridge, Nordic Concr. Res. 3 (1984) 140–166.
[7] L.E. Borgman, Statistical models for ocean waves and wave forces, Advances in Hydroscience vol. 8, Elsevier, 1972, pp. 139–181, https://doi.org/10.1016/B978-0-12-021808-0.50008-5.
[8] B.L. Hutchison, Impulse response techniques for floating bridges and breakwaters subject to short-crested seas, Mar. Technol. 21 (3) (1984) 270–276.
[9] B. Villoria, Floating bridge technology – prediction of extreme environmental load effects, Proceedings of the 35th International Conference on Ocean, Offshore and Arctic Engineering, ASME, 2016, pp. 1–8, , https://doi.org/10.1115/OMAE2016-54433.
[10] T. Moan, Z. Gao, E. Ayala-Uraga, Uncertainty of wave-induced response of marine structures due to long-term variation of extratropical wave conditions, Mar. Struct. 18 (4) (2005) 359–382, https://doi.org/10.1016/j.marstruc.2005.11.001.
[11] E.M. Bitner-Gregersen, K.C. Ewans, M.C. Johnson, Some uncertainties associated with wind and wave description and their importance for engineering applications, Ocean Eng. 86 (2014) 11–25, https://doi.org/10.1016/j.oceaneng.2014.05.002.
[12] K.A. Kvåle, O. Øiseth, Characterization of the Wave Field Around an Existing End-Supported Pontoon Bridge from Simulated Data, Springer International Publishing, 2019, pp. 345–359, https://doi.org/10.1007/978-3-319-78187-7_26.
[13] F.-I.G. Giske, K.A. Kvåle, B.J. Leira, O. Øiseth, Long-term extreme response analysis of a long-span pontoon bridge, Mar. Struct. 58 (2018) 154–171, https://doi.org/10.1016/j.marstruc.2017.11.010.
[14] F.-I.G. Giske, B.J. Leira, O. Øiseth, Long-term extreme response analysis of marine structures using inverse SORM, J. Offshore Mech. Arctic Eng. 140 (5) (2018) 1–8, https://doi.org/10.1115/1.4039718.
[15] O. Øiseth, A. Rönnquist, A. Naess, R. Sigbjörnsson, Estimation of extreme response of floating bridges by Monte Carlo simulation, Proceedings of the 9th International Conference on Structural Dynamics, EURODYN (2014) 2905–2912.
[16] A. Naess, O. Gaidai, Estimation of extreme values from sampled time series, Struct. Saf. 31 (4) (2009) 325–334, https://doi.org/10.1016/j.strusafe.2008.06.021.
[17] Y. Xu, O. Øiseth, A. Naess, T. Moan, Prediction of long-term extreme load effects due to wind for cable-supported bridges using time-domain simulations, Eng. Struct. 148 (2017) 239–253, https://doi.org/10.1016/j.engstruct.2017.06.051.
[18] Statens Vegvesen, Curved Bridge – Navigation Channel in South, Oslo, Norway, (2016) Report No. NOT-KTEKA-021.
[19] SINTEF Ocean, SIMO 4.10.0 Theory Manual, Trondheim, Norway, (2017).
[20] SINTEF Ocean, RIFLEX 4.10.0 Theory Manual, Trondheim, Norway, (2017).

[21] W.E. Cummins, The Impulse Response Function and Ship Motions, Washington DC, USA, (1962) Report No. DTMB-1661.
[22] L.J. Tick, Differential equations with frequency-dependent coefficients, J. Ship Res. 3 (1959) 45–46.
[23] K. Hasselmann, T.P. Barnett, E. Bouws, H. Carlson, D.E. Cartwright, K. Enke, J.A. Ewing, H. Gienapp, D.E. Hasselmann, P. Kruseman, A. Meerburg, P. Muller, D.J. Olbers, K. Richter, W. Sell, H. Walden, Measurements of wind-wave growth and swell decay during the Joint North Sea Wave Project (JONSWAP), Dtsch Hydrogr. Z. 8 (12) (1973).
[24] D.N.V. Wadam, Wave Analysis by Diffraction and Morison Theory, SESAM User Manual, Høvik, Norway, (2014) Report no. 94-7100.
[25] K.A. Kvåle, R. Sigbjörnsson, O. Øiseth, Modelling the stochastic dynamic behaviour of a pontoon bridge: a case study, Comput. Struct. 165 (2016) 123–135, https://doi.org/10.1016/j.compstruc.2015.12.009.
[26] X. Xiang, Maneuvering of Two Interacting Ships in Waves (Ph.D. thesis), Norwegian University of Science and Technology, 2012, https://brage.bibsys.no/xmlui/handle/11250/238361.
[27] X. Xiang, T. Viuff, B. Leira, O. Øiseth, Impact of hydrodynamic interaction between pontoons on global responses of a long floating bridge under wind waves, Proceedings of the 37th International Conference on Ocean, Offshore and Arctic Engineering (2018) 1–11, https://doi.org/10.1115/OMAE2018-78625.
[28] M.S. Seif, Y. Inoue, Dynamic analysis of floating bridges, Mar. Struct. 11 (1–2) (1998) 29–46, https://doi.org/10.1016/S0951-8339(97)00012-9.
[29] Statens Vegvesen, Design Basis, Oslo, Norway, (2016) Report No. RAP-GEN-001.
[30] J. Wang, E. Cheynet, J. Snæbjörnsson, J.B. Jakobsen, Coupled aerodynamic and hydrodynamic response of a long span bridge suspended from floating towers, J. Wind Eng. Ind. Aerodyn. 177 (2018) 19–31, https://doi.org/10.1016/j.jweia.2018.03.024.
[31] A. Naess, T. Moan, Stochastic Dynamics of Marine Structures, Cambridge University Press, 2013.
[32] R.D. Cook, D.S. Malkus, M.E. Plesha, R.J. Witt, Concepts and Applications of Finite Element Analysis, John Wiley & Sons, Inc., 2002.
[33] J. Fish, T. Belytschko, A First Course in Finite Elements, John Wiley & Sons, Ltd., 2007.
[34] R.M. Larssen, S.N. Remseth, B.J. Leira, Parameter sensitivity of predicted extreme response for a submerged tubular bridge, Proceedings of the 3rd symposium on strait crossings, Balkema Publishers, Rotterdam, 1994, pp. 607–613.
[35] L. Damkilde, Stress and Stiffness Analysis of Beam-Sections, Technical University of Denmark, 2000.
[36] N. Spidsøe, D.N. Karunakaran, Nonlinear dynamic behaviour of jack-up platforms, Mar. Struct. 9 (1) (1996) 71–100, https://doi.org/10.1016/0951-8339(95)00005-Q.
[37] K.-A. Farnes, T. Moan, Extreme dynamic, non-linear response of fixed platforms using a complete long-term approach, Appl. Ocean Res. 15 (6) (1993) 317–326, https://doi.org/10.1016/0141-1187(93)90001-E.
[38] P. Fu, B.J. Leira, D. Myrhaug, Assessment of Methods for Short-Term Extreme Value Analysis of Riser Collision, (2018), pp. 1–9, https://doi.org/10.1115/OMAE2018-78318.
[39] P. Brodtkorb, P. Johannesson, G. Lindgren, I. Rychlik, J. Rydén, E. Sjö, WAFO – a matlab toolbox for the analysis of random waves and loads, Proc. 10'th Int. Offshore and Polar Eng. Conf., ISOPE, Seattle, USA (2000) 343–350.
[40] S.N. Remseth, B.J. Leira, K.M. Okstad, K.M. Mathisen, T. Haukås, Dynamic response and fluid/structure interaction of submerged floating tunnels, Comput. Struct. 72 (4) (1999) 659–685, https://doi.org/10.1016/S0045-7949(98)00329-0.